ACS APPLIED MATERIALS & INTERFACES

Research Article

www.acsami.org

# Two-Dimensional $V_2O_5$ Sheet Network as Electrode for Lithium-Ion Batteries

Yun Xu,[†] Marco Dunwell,[†] Ling Fei,[†] Engang Fu,[‡] Qianglu Lin,[†] Brian Patterson,[†] Bin Yuan,[†] Shuguang Deng,[†] Paul Andersen,[†] Hongmei Luo,*[,†] and Guifu Zou*[,§]

[†]Department of Chemical and Materials Engineering, New Mexico State University, New Mexico 88003, United States

[‡]State Key Laboratory of Nuclear Physics and Technology, School of Physics, Peking University, Beijing 100871, P.R. China

[§]College of Physics, Optoelectronics and Energy & Collaborative Innovation Center of Suzhou Nano Science and Technology, Soochow University, Suzhou 215000, P.R. China

Supporting Information

**ABSTRACT:** Two-dimensional $V_2O_5$ and manganese-doped $V_2O_5$ sheet network were synthesized by a one-step polymer-assisted chemical solution method and characterized by X-ray diffraction, scanning electron microscopy, transmission electron microscopy, thermal-gravimetric analysis, and galvanostatic discharge−charge analysis. The $V_2O_5$ particles were covered with thin carbon layers, which remained after decomposition of the polymer, forming a network-like sheet structure. This $V_2O_5$ network exhibits a high capacity of about 300 and 600 mA·h/g at a current density of 100 mA/g when it was used as a cathode and anode, respectively. After doping with 5% molar ratio of manganese, the capacity of the cathode increases from 99 to 165 mA·h/g at a current density of 1 A/g (~3 C). This unique network structure provides an interconnected transportation pathway for lithium ions. Improvement of electrochemical performance after doping manganese could be attributed to the enhancement of electronic conductivity.

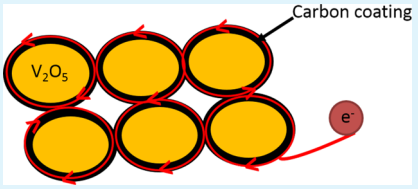


**KEYWORDS:** *$V_2O_5$ network, manganese-doped, lithium-ion battery, polymer-assisted solution method, conductivity*

## 1. INTRODUCTION

Rechargeable lithium-ion batteries have been extensively investigated for their promising application in hybrid electric vehicles because of their high energy and power densities and long cycle lifetime. To obtain high-energy lithium-ion batteries, the performance of cathodes should match the high capacity of anodes. A variety of compounds have been investigated as cathode materials for lithium-ion batteries, including $LiFePO_4$, $LiMn_2O_4$, $LiCoO_2$, and $V_2O_5$ as well.[1−5] Among which $V_2O_5$ has been extensively investigated as an electrode material because of its high capacity and low cost.[6−9] $V_2O_5$ has a crystal structure formed by stacking $V_2O_5$ layers perpendicular to the *c*-axis via van der Waals interactions. This typical layered crystal structure makes reversible insertion and extraction of lithium ions quite feasible. By insertion of two lithium ions, the theoretical capacity of $V_2O_5$ is as high as 290 mA·h/g. This is much higher than the capacities of more commonly used cathode materials such as $LiFePO_4$ (170 mA·h/g), $LiCoO_2$ (140 mA·h/g), and $LiMn_2O_4$ (148 mA·h/g), making $V_2O_5$ a promising cathode material. Moreover, $V_2O_5$ can also serve as the anode material for lithium-ion batteries.[7] However, the application of $V_2O_5$ is still greatly hindered by its poor stability and slow kinetics resulting from electronic and ionic conductivity.[10,11] So far, various $V_2O_5$ nanostructures have been reported to be helpful in improving the electrochemical performance.[6,8,10,12−14] For example, ultralong hierarchical $V_2O_5$ nanowires fabricated by electrospinning showed a capacity of 187 mA·h/g after 50 cycles at 30 mA/g.[15] Carbon-supported metal oxides have been intensively studied to improve the performance.[16−20] Many carbonaceous $V_2O_5$ composites have been reported to improve the electrical conductivity and cycle performance.[21−24] Carbon-coated $V_2O_5$ nanocrystals give an impressive rate performance of 288 mA·h/g at 1 A/g.[16]

It is believed that two-dimensional (2D) nanomaterials can offer a robust skeleton and a continuous pathway for lithium ions.[25−27] $V_2O_5$ nanowire networks were reported to have a capacity of 240 mA·h/g at 500 mA/g.[14] On the other hand, doping of transition-metal ions has been studied to improve the electrochemical performance of $V_2O_5$. When cations are doped with different valences, electrochemical performance is improved significantly and the electronic conductivity can be increased by a factor of $10^4$.[28−32] In this study, we report an easy and economical way for making a $V_2O_5$ sheet network structure from one-step polymer-assisted solution method that provides interconnected channels for effective ion transportation. In the meantime, a layer of carbon formed on the surface of $V_2O_5$ sheet directly from decomposition of polymer. Charge transfer is greatly enhanced by carbon layer and 2D network structure. Both the anode and cathode performance of $V_2O_5$ were investigated. Furthermore, the samples after doping

Received: September 2, 2014
Accepted: November 4, 2014
Published: November 4, 2014

  

manganese show an improved conductivity and a higher capacity.

## 2. EXPERIMENTAL SECTION

Commercially available ammonium metavanadate ($NH_4VO_3$, 0.4 g) was dissolved in 10 mL of deionized water with the addition of 2 mL of hydrogen peroxide (30%). Two grams of polyethylenimine (PEI, 50 wt %) and 1 g of ethylenediaminetetraacetic acid (EDTA) were dissolved in 10 mL of deionized water. Then this polymer solution was added to the as-prepared vanadium solution. Two milliliters of ammonium hydroxide (31 wt %) was dropped to get a clear solution. The well-mixed solution was then transferred to a furnace in a 50 mL ceramic container and heated at 1 °C/min at 550 or 650 °C for 3 h. Manganese-doped $V_2O_5$ (Mn−$V_2O_5$) was prepared by dropping the different amounts (5 and 10 mol %) of manganese acetate solution (1 M) into the vanadium solution, followed by the same heating process as for $V_2O_5$. For comparison, $V_2O_5$ nanoparticles were also synthesized by a hydrothermal method: the vanadium solution was prepared in the same way we described above. The solution was transferred to a 40 mL hydrothermal Teflon vessel and reacted at 200 °C for 18 h.

The structure and morphology of the as-prepared samples were characterized by X-ray diffraction (XRD; Cu K$\alpha$, radiation), field emission scanning electron microscopy (JEOL-7500, 2 kV), and transmission electron microscopy (TEM; JEOL-2010, 200 kV). The carbon content was determined by a Perkin-Elmer Pyris 1 thermogravimetric analyzer (TGA) at a heating rate of 10 °C $min^{-1}$ in air. Electrochemical measurements were carried out using CR-2032 coin cells. For the preparation of the working electrode, a mixture of $V_2O_5$, carbon black, and polyvinylidene fluoride in a weight ratio of 70:20:10 were mixed with 1-methy1-2-pyrrolidone to make a slurry. The slurry was casted onto an aluminum collector to serve as the cathode and to a nickel foam collector for the anode. Before assembly of coin cells, electrodes were dried at 70 °C overnight. All the samples were weighted by a microbalance (Denver Instrument SI-215D) with an accuracy of 0.01 mg. The loading weight for the electrodes is around 1 mg. Lithium foil was used as the counter electrode. A solution of 1 M $LiPF_6$ in ethylene carbonate/dimethyl carbonate (1:1 in volume) was used as the electrolyte. Coin cell assembly was carried out in an argon-filled glovebox with an oxygen concentration below 1 ppm. Charge/discharge measurements were performed using a Land battery testing system. Cyclic voltammograms and the electrochemical impedance were collected on a Princeton Applied Research Versa STAT4 electrochemical workstation and a CHI-680A (CH Instruments, Inc.) workstation, respectively.

## 3. RESULTS AND DISCUSSION

The XRD patterns of pure $V_2O_5$ in Figure 1 show that all the peaks can be indexed to orthorhombic $V_2O_5$ phase (JCPDS 41-1426), and the sample annealed at 650 °C has better crystallinity than the sample annealed at 550 °C. The XRD pattern of 5% Mn−$V_2O_5$ shows the formation of $MnV_2O_6$ (JCPDS 35-0139) together with the main phase $V_2O_5$. In the case of 10% Mn−$V_2O_5$, peak intensity increases, indicating the increased amount of $MnV_2O_6$ in the product. As shown in Figure 2, SEM and TEM images of $V_2O_5$ annealed at 550 °C show that $V_2O_5$ forms a sheetlike structure and the particles

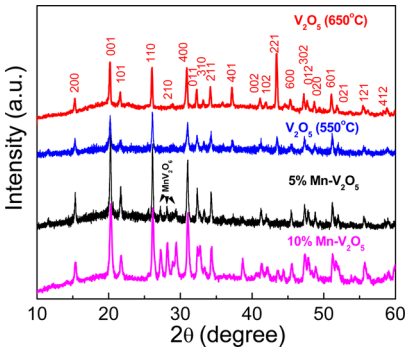


**Figure 1.** XRD patterns of $V_2O_5$ annealed at 550 and 650 °C and Mn(5%,10%)−$V_2O_5$ annealed at 550 °C.

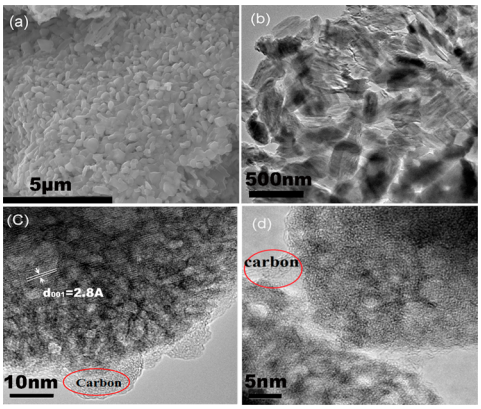


**Figure 2.** SEM (a), TEM (b), and HRTEM (c,d) images of $V_2O_5$ network annealed at 550 °C.

connected to each other. The lattice distance measured in Figure 2c is 2.8 Å corresponding to the (001) plane of $V_2O_5$. As revealed by high-resolution TEM (HRTEM) images, a thin layer of amorphous carbon was observed on the surface of $V_2O_5$ and the $V_2O_5$ sheets are actually connected by amorphous carbon which was formed during the decomposition of EDTA and PEI. EDTA and PEI potentially serve as the initial network in the preparation process, efficiently preventing aggregation of the particles.[33,34] While $V_2O_5$ annealed at 650 °C is highly crystalline with a layered crystal structure, as shown in the TEM images (Figure S1 of the Supporting Information) with no carbon observed. The SEM image in Figure S1a reveals that $V_2O_5$ lost network structure when it was annealed at 650 °C. TGA (Figure S2) demonstrated that the carbon is around 3 wt % in the $V_2O_5$ annealed at 550 °C. However, no obvious weight loss was observed for $V_2O_5$ annealed at 650 °C, indicating complete removal of EDTA and PEI at 650 °C. In addition, $V_2O_5$ annealed at 650 °C might have gone through a process of melting and recrystallization due to the low melting point of bulk $V_2O_5$ (690 °C),[35] since different-sized sheets were observed in the SEM image (Figure S1a).

To investigate $V_2O_5$ network's reversibility, stability, and rate capability in charge/discharge performance, galvanostatic measurements were applied accordingly. The capacity was calculated based on the mass of $V_2O_5$. Figure 3a shows the cycle performance of $V_2O_5$ annealed at 550 °C at different current densities of 400 and 800 mA/g in a voltage range of 2−4 V. Average capacities of 219 and 143 mA·h/g were delivered, respectively, for 50 cycles. At a current density of 800 mA/g, $V_2O_5$ annealed at 650 °C gave a capacity only around 20 mA·h/


dx.doi.org/10.1021/am505975n | ACS Appl. Mater. Interfaces 2014, 6, 20408−20413

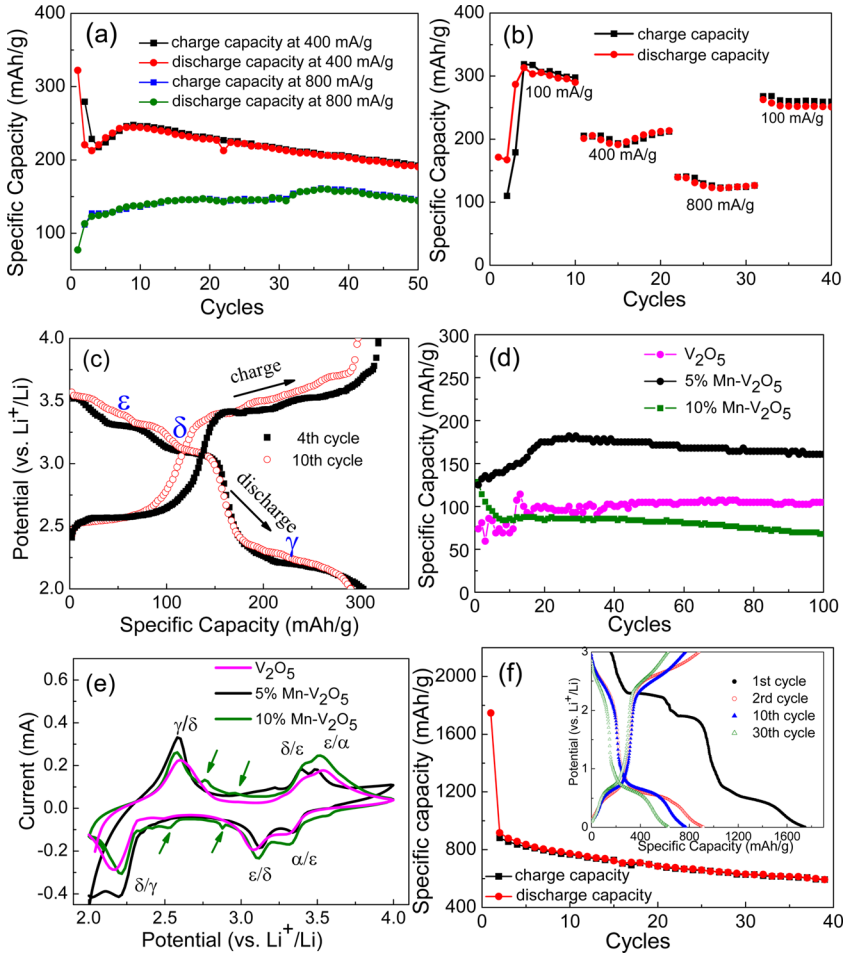


**Figure 3.** (a) Cycle performance of $V_2O_5$ network cathode annealed at 550 °C at current densities of 400 and 800 mA/g; (b) rate performance of $V_2O_5$; (c) charge and discharge curves of the 4th and 10th cycles; (d) cyclic voltammetry of doped and pure $V_2O_5$ network; (e) cycle performance of doped and pure $V_2O_5$ network at a current density of 1 A/g; and (f) anode performance of pure $V_2O_5$ network at a current density of 100 mA/g. Inset is the voltage profiles of the 1st, 2nd, 10th, and 30th cycles.

g (see Figure 4a), while the nanoparticles synthesized hydrothermally with diameters of about 100 nm (Figure S1d)

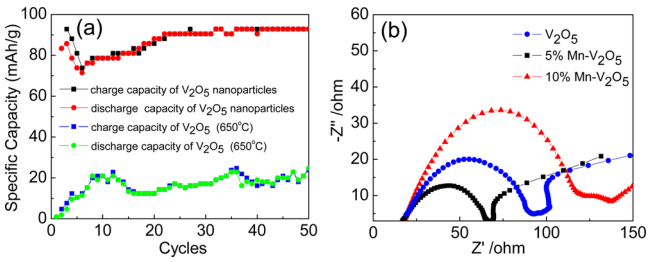


**Figure 4.** (a) Cycle performance of hydrothermal $V_2O_5$ nanoparticles and $V_2O_5$ annealed at 650 °C at a current density of 800 mA/g. (b) Impedance spectra of the three samples with different dopant amounts.

showed an average capacity of 87 mA·h/g (Figure 4a). The above result shows that network structure gives the highest capacity. The difference in the cycle performance could be attributed to the fact that the network structure provides a much more continuous pathway for the diffusion of lithium ions. Furthermore, the existence of carbon on the surface of particles increases the conductivity. In this case, carbon acts as a bridge to connect the particles, as well as the protective shell layer to alleviate the volume change of $V_2O_5$ during the charge and discharge processes.

Rate performance of $V_2O_5$ cathode was tested at increasing current densities of 100, 400, and 800 mA/g in the voltage range of 2−4 V, as shown in Figure 3b. The electrode has a capacity of around 300 mA·h/g at a current density of 100 mA/g, which is almost the same as the theoretical capacity of 297 mA·h/g (corresponding to insertion/extraction of two lithium ions). The electrode delivered stable capacities at current densities of 400 and 800 mA/g. Furthermore, when the current density decreased from 800 to 100 mA/g, the capacity was maintained around 260 mA·h/g.

Figure 3c shows the potential versus capacity curves in voltage ranges of 2−4 V at a current density of 100 mA/g. It took a couple of cycles for the electrolyte to penetrate into the electrode, so the fourth cycle charge and discharge curve are shown. The typical plateaus corresponding to the phase transitions of crystalline $V_2O_5$ are obvious. The plateaus at approximately 3.4, 3.1, and 2.3 V can be attributed to consecutive insertion of lithium ions to form $\varepsilon$-$Li_{0.5}V_2O_5$, $\delta$-$LiV_2O_5$, and $\gamma$-$Li_2V_2O_5$, respectively. The reactions that happened at these potentials are described in the following equations,

$$V_2O_5 + 0.5Li^+ + 0.5e^- \leftrightarrow \varepsilon - Li_{0.5}V_2O_5 \quad (1)$$

$$Li_{0.5}V_2O_5 + 0.5Li^+ + 0.5e^- \leftrightarrow \delta - LiV_2O_5 \quad (2)$$

$$LiV_2O_5 + Li^+ + e^- \leftrightarrow \gamma - Li_2V_2O_5 \quad (3)$$

At the 10th cycle, the charge/discharge curve displays almost the same shape as the fourth cycle, suggesting that the charge and discharge processes are highly reversible. This reversibility comes from the unique 2D network structure as well as the carbon coating on the particles' surface which could maintain the structure during lithium insertion and extraction. Besides, this layered structure is very feasible for the lithium ions to insert within the layers. The fast electronic kinetics is associated with the hierarchical layered structure from the macroscale of the network to the nanoscale of the crystal structure.

To further improve the performance of $V_2O_5$, Mn was doped into the network, which was expected to improve the electronic conductivity. Effect of Mn dopant was investigated by doping with different amounts of Mn into $V_2O_5$. The cycle performances of doped $V_2O_5$ were compared with the $V_2O_5$ network at a current density of 1 A/g as shown in Figure 3d. 5% Mn−$V_2O_5$ delivers a larger average capacity of 165 mA·h/g compared to 99 mA·h/g for $V_2O_5$. The sample showed an increase for the initial few cycles for two reasons. First, it took a few cycles to activate the electrode materials thoroughly. Second, there is a possibility that Mn ions sit in the layers of $V_2O_5$ and they are driven away after lithium ions inserted, and then the rooms for lithium ions become larger, leading to an increase of the capacity. Also, the capacity for 5% Mn−$V_2O_5$ is very stable until the 100th cycle. The capacity is higher than the Mn-doped $V_2O_5$ film reported by Yu et al. The film delivered a capacity of 150 mA·h/g at a current density of 680 mA/g.[23] However, if we increase the Mn content to 10%, the performance cannot even match the pure $V_2O_5$. The capacity also slightly decreased along cycles. The possible reason for the improvement of 5% Mn−$V_2O_5$ is that oxygen vacancies were formed after doping low-valence Mn. The assumption is manganese substitutes vanadium and forms oxygen vacancies as described by Yu et al.[29] Oxygen vacancies are formed by the suggested reaction as[29]

$$Mn^{2+} + \frac{1}{2}V_2O_5 \rightarrow Mn_V'' + \frac{5}{2}V_O^{\cdot\cdot}$$

in which $Mn_V''$ is a manganese substitutional defect and $V_{\ddot{o}}$ is oxygen vacancy. These vacancies will lead to a more open structure and favor the diffusion of lithium ions by the vacancy exchange mechanism, thereby increasing the ionic conductivity. In contrast, excessive 10 % Mn will lead to the formation of impurity of $MnV_2O_6$ and block the diffusion pathway of lithium ions.

Cyclic voltammograms of $V_2O_5$ and doped $V_2O_5$ (Figure 3e) were measured at a scan rate of 1 mV/s in the potential range of 2.0 to 4 V (vs $Li^+$/Li). All of the three samples exhibited the typical redox peaks of $V_2O_5$ during delithiation. The redox peaks at 3.5/3.3, 3.4/3.1, and 2.57/2.2 V match well with the voltage profile and corresponds to the formation of different phase transformations of $\varepsilon/\alpha$, $\delta/\varepsilon$, and $\gamma/\delta$, respectively. However, for the sample doped with 10% Mn, extra peaks pointed by green arrows are attributed to the reaction of $MnV_2O_6$ with lithium ions. By integrating peak area, we can estimate the content of $MnV_2O_6$ in the samples. The content of $MnV_2O_6$ in sample 5% Mn−$V_2O_5$ is neglected because no reaction peak from $MnV_2O_6$ was detected. For sample 10% Mn−$V_2O_5$, the content of $MnV_2O_6$ is estimated to be 6% and the rest is $V_2O_5$. If we note the reduction peak at 3.3 V as $\varepsilon$-peak and reduction peak at 3.1 V as $\delta$-peak, where $V^{5+}$ is reduced to $V^{4+}$, we found that 5% Mn−$V_2O_5$ has a smaller peak current compared to $V_2O_5$ and 10% Mn−$V_2O_5$, indicating a larger amount of $V^{4+}$ existing in 5% Mn−$V_2O_5$. More $V^{4+}$ means higher electronic conductivity.[12]

To gain insight into the effect of Mn doping, we took the electrochemical impedance spectroscopy measurements for the samples with a different amount of doping as shown in Figure 4b. Comparing the diameter of the semicircle in a high-frequency region, the polarization resistance is the smallest for $V_2O_5$ (5% Mn) and the largest for $V_2O_5$ (10% Mn).

There were a few reports on anode performance of $V_2O_5$ probably because of the relatively high intercalation potential for $V_2O_5$.[7,36] Liu et al. reported the anode and cathode performance of $V_2O_5$ with $SnO_2$ (10−15 wt %) double-shelled nanocapsules.[7] Such composites exhibited high reversible capacity and good rate capability due to the hollow architecture provides short lithium ion pathways and easily accommodates large volume change.[7] Wong and co-workers tested the cathode and anode performance of $V_2O_5$ nanobelts on titanium substrate.[36] The anode showed good rate capability due to the direct contact between the substrate and $V_2O_5$.[36] The ability of the $V_2O_5$ network as an anode material was also verified in this paper. The cell was tested in a voltage range of 0.005−3 V at a current density of 100 mA/g, as shown in Figure 3f. The inset of Figure 3f is the voltage profiles of the 1st, 2nd, 10th, and 30th cycles. The first discharge and charge capacity are 1747 and 880 mA·h/g with an irreversible capacity loss of 49%. The anode delivers a capacity of 600 mA·h/g after 40 cycles. From the potential vs capacity curve we can observe that, in the first discharge curve, plateaus appear at approximately 2.3 and 1.9 V, corresponding to the formation of $\gamma$-$Li_2V_2O_5$ and lithium-rich $\omega$-$Li_3V_2O_5$, respectively. The reaction that happens at 1.9 V is described in the following equation:

$$\gamma\text{-}Li_2V_2O_5 + Li^+ + e^- \rightarrow \omega\text{-}Li_3V_2O_5 \quad (4)$$

The first irreversible capacity is due to the formation of a solid electrolyte interface via the electrolyte decomposition during the first discharge.[7,36] The plateau at 1.9 V could not be recovered in the following cycles. The irreversible capacity at the following cycles is because lithium ions could not be removed upon the formation of $\omega$-$Li_3V_2O_5$.[6]

## 4. CONCLUSION

A high-performance 2D $V_2O_5$ network for lithium-ion batteries was synthesized by a one-step polymer-assisted chemical solution method. The 2D network structure delivers high capacity and excellent stability, which are attributed to the continuous pathway for the lithium ions and rapid electrolyte diffusion. Mn-doped $V_2O_5$ results in the enhancement of lithium ion diffusion, demonstrated by both impedance and rate performance. This improvement can be explained by the enhancement of electronic conductivity. However, excessive Mn leads to a deterioration of battery performances because of the unwanted phase formation and lower conductivity. This facile method can be applied to the synthesis of many other metal oxide networks to achieve a high performance in lithium-ion batteries.

## ■ ASSOCIATED CONTENT

### Supporting Information

(Figure S1) Morphology characterization of $V_2O_5$ annealed at 650 °C and $V_2O_5$ nanoparticles by hydrothermal method. (Figure S2) TGA analysis of $V_2O_5$ annealed at 550 and 650 °C. This material is available free of charge via the Internet at http://pubs.acs.org/.

## ■ AUTHOR INFORMATION

### Corresponding Authors

*Tel.: 575-646-4204. Fax: 575-646-7706. E-mail: hluo@nmsu.edu (H. Luo).
*Tel.: +86-512-65228130. Fax: +86-512-65228130. E-mail: zouguifu@suda.edu.cn (G. Zou).

### Notes

The authors declare no competing financial interest.

## ■ ACKNOWLEDGMENTS

H.L. acknowledges the support from the National Science Foundation under Grant 1131290. Y.X. acknowledges the support from New Mexico Consortium (NMC) and Los Alamos National Laboratory (LANL). G.Z. acknowledges the support from the National Natural Science Foundation of China (21101110), Jiangsu Fund for Distinguished Young Scientist (BK20140010), Jiangsu Specially-Appointed Professor Program (SR1080042), and Jiangsu Scientific and Technological Innovation Team (2013).

## ■ REFERENCES

(1) Teshima, K.; Lee, S.; Mizuno, Y.; Inagaki, H.; Hozumi, M.; Kohama, K.; Yubuta, K.; Shishido, T.; Oishi, S. Environmentally Friendly Growth of Well-Developed $LiCoO_2$ Crystals for Lithium-Ion Rechargeable Batteries Using a NaCl Flux. *Cryst. Growth Des.* **2010**, *10*, 4471−4475.
(2) Sun, C.; Rajasekhara, S.; Goodenough, J. B.; Zhou, F. Monodisperse Porous $LiFePO_4$ Microspheres for a High Power Li-Ion Battery Cathode. *J. Am. Chem. Soc.* **2011**, *133*, 2132−2135.
(3) Shaju, K. M.; Bruce, P. G. A Stoichiometric Nano-$LiMn_2O_4$ Spinel Electrode Exhibiting High Power and Stable Cycling. *Chem. Mater.* **2008**, *20*, 5557−5562.
(4) Lim, S.; Yoon, C. S.; Cho, J. Synthesis of Nanowire and Hollow $LiFePO_4$ Cathodes for High-Performance Lithium Batteries. *Chem. Mater.* **2008**, *20*, 4560−4564.
(5) Xu, Y.; Chen, G.; Fu, E.; Zhou, M.; Dunwell, M.; Fei, L.; Deng, S.; Andersen, P.; Wang, Y.; Jia, Q.; Luo, H. Nickel Substituted $LiMn_2O_4$ Cathode with Durable High-rate Capability for Li-ion Batteries. *RSC Adv.* **2013**, *3*, 18441−18445.
(6) Chan, C. K.; Peng, H.; Twesten, R. D.; Jarausch, K.; Zhang, X. F.; Cui, Y. Fast, Completely Reversible Li Insertion in Vanadium Pentoxide Nanoribbons. *Nano Lett.* **2007**, *7*, 490−495.
(7) Liu, J.; Xia, H.; Xue, D.; Lu, L. Double-Shelled Nanocapsules of $V_2O_5$-Based Composites as High-Performance Anode and Cathode Materials for Li Ion Batteries. *J. Am. Chem. Soc.* **2009**, *131*, 12086−12087.
(8) Wang, Y.; Zhang, H. J.; Siah, K. W.; Wong, C. C.; Lin, J.; Borgna, A. One Pot Synthesis of Self-assembled $V_2O_5$ Nanobelt Membrane-viacapsule-like Hydrated Precursor as Improved Cathode for Li-ion Battery. *J. Mater. Chem.* **2011**, *21*, 10336−10341.
(9) Lee, J.; Pennycook, S. J.; Pantelides, S. T. Simultaneous Enhancement of Electronic and Li+ Ion Conductivity in $LiFePO_4$. *Appl. Phys. Lett.* **2012**, *101*, 033901.
(10) Chou, S.-L.; Wang, J.-Z.; Sun, J.-Z.; Wexler, D.; Forsyth, M.; Liu, H.-K.; MacFarlane, D. R.; Dou, S.-X. High Capacity, Safety, and Enhanced Cyclability of Lithium Metal Battery Using a $V_2O_5$ Nanomaterial Cathode and Room Temperature Ionic Liquid Electrolyte. *Chem. Mater.* **2008**, *20*, 7044−7051.
(11) Gregoire, G.; Baffier, N.; Kahn-harari, A.; Badot, J.-c. X-Ray Powder Diffraction Study of a New Vanadium Oxide $Cr_{0.11}V_2O_{5.16}$ Synthesized by a Sol-gel Process. *J. Mater. Chem.* **1998**, *8*, 2103−2108.
(12) Liu, D.; Liu, Y.; Garcia, B. B.; Zhang, Q.; Pan, A.; Jeong, Y.-H.; Cao, G. $V_2O_5$ Xerogel Electrodes with Much Enhanced Lithium-ion Intercalation Properties with $N_2$ Annealing. *J. Mater. Chem.* **2009**, *19*, 8789−8795.
(13) Liu, J.; Zhou, Y.; Wang, J.; Pan, Y.; Xue, D. Template-free Solvothermal Synthesis of Yolk-shell $V_2O_5$ Microspheres as Cathode Materials for Li-ion Batteries. *Chem. Commun.* **2011**, *47*, 10380−10382.
(14) Ni, S.; Zeng, H.; Yang, X. Fabrication of $VO_2$ (B) Nanobelts and Their Application in Lithium Ion Batteries. *J. Nanomater.* **2011**, *2011*, Article ID 961389, doi 10.1155/2011/961389.
(15) Mai, L.; Xu, L.; Han, C.; Xu, X.; Luo, Y.; Zhao, S.; Zhao, Y. Electrospun Ultralong Hierarchical Vanadium Oxide Nanowires with High Performance for Lithium Ion Batteries. *Nano Lett.* **2010**, *10*, 4750−4755.
(16) Zhang, X.-F.; Wang, K.-X.; Wei, X.; Chen, J.-S. Carbon-Coated $V_2O_5$ Nanocrystals as High Performance Cathode Material for Lithium Ion Batteries. *Chem. Mater.* **2011**, *23*, 5290−5292.
(17) Xu, Y.; Yi, R.; Yuan, B.; Wu, X.; Dunwell, M.; Lin, Q.; Fei, L.; Deng, S.; Andersen, P.; Wang, D.; Luo, H. High Capacity $MoO_2$/Graphite Oxide Composite Anode for Lithium-Ion Batteries. *J. Phys. Chem. Lett.* **2012**, *3*, 309−314.
(18) Du, G.; Seng, K. H.; Guo, Z.; Liu, J.; Li, W.; Jia, D.; Cook, C.; Liu, Z.; Liu, H. Graphene-$V_2O_5{\cdot}nH_2O$ Xerogel Composite Cathodes for Lithium Ion Batteries. *RSC Adv.* **2011**, *1*, 690−697.
(19) Yamada, H.; Tagawa, K.; Komatsu, M.; Moriguchi, I.; Kudo, T. High Power Battery Electrodes Using Nanoporous $V_2O_5$/Carbon Composites. *J. Phys. Chem. C* **2007**, *111*, 8397−8402.
(20) Kim, D.; Yun, J.; Lee, G.; Ha, J. S. Fabrication of High Performance Flexible Micro-Supercapacitor Arrays with Hybrid Electrodes of MWNT/$V_2O_5$ Nanowires Integrated with a $SnO_2$ Nanowire UV Sensor. *Nanoscale* **2014**, *6*, 12034−12041.
(21) Zhou, X.; Wu, G.; Wu, J.; Yang, H.; Wang, J.; Gao, G.; Cai, R.; Yan, Q. Multiwalled Carbon Nanotubes-$V_2O_5$ Integrated Composite with Nanosized Architecture as a Cathode Material for High Performance Lithium Ion Batteries. *J. Mater. Chem. A* **2013**, *1*, 15459−15468.
(22) Tan, H. T.; Rui, X.; Yu, H.; Liu, W.; Xu, C.; Xu, Z.; Hng, H. H.; Yan, Q. Aqueous-Based Chemical Route toward Ambient Preparation of Multicomponent Core−Shell Nanotubes. *ACS Nano* **2014**, *8*, 4004−4014.
(23) Cheng, J.; Wang, B.; Xin, H. L.; Yang, G.; Cai, H.; Nie, F.; Huang, H. Self-assembled $V_2O_5$ Nanosheets/Reduced Graphene Oxide Hierarchical Nanocomposite as a High-Performance Cathode Material for Lithium Ion Batteries. *J. Mater. Chem. A* **2013**, *1*, 10814−10820.
(24) Chen, D.; Yi, R.; Chen, S.; Xu, T.; Gordin, M. L.; Lv, D.; Wang, D. Solvothermal Synthesis of $V_2O_5$/Graphene Nanocomposites for High Performance Lithium Ion Batteries. *Mater. Sci. Eng. B* **2014**, *185*, 7−12.
(25) Luo, B.; Fang, Y.; Wang, B.; Zhou, J.; Song, H.; Zhi, L. Two Dimensional Graphene-$SnS_2$ Hybrids with Superior Rate Capability for Lithium Ion Storage. *Energy Environ. Sci.* **2012**, *5*, 5226−5230.
(26) Xie, J.; Yang, X.; Zhou, S.; Wang, D. Comparing One- and Two-Dimensional Heteronanostructures as Silicon-Based Lithium Ion Battery Anode Materials. *ACS Nano* **2011**, *5*, 9225−9231.
(27) Ostreng, E.; Gandrud, K. B.; Hu, Y.; Nilsen, O.; Fjellvag, H. High Power Nano-structured $V_2O_5$ Thin Film Cathodes by Atomic Layer Deposition. *J. Mater. Chem. A* **2014**, *2*, 15044−15051.
(28) Wei, Y.; Ryu, C.-W.; Kim, K.-B. Cu-Doped $V_2O_5$ as a High-Energy Density Cathode Material for Rechargeable Lithium Batteries. *J. Alloys Compd.* **2008**, *459*, L13−L17.
(29) Yu, D. M.; Zhang, S. T.; Liu, D. W.; Zhou, X. Y.; Xie, S. H.; Zhang, Q. F.; Liu, Y. Y.; Cao, G. Z. Effect of Manganese Doping on Li-

Ion Intercalation Properties of $V_2O_5$ Films. *J. Mater. Chem.* **2010**, *20*, 10841−10846.
(30) Coustier, F.; Passerini, S.; Smyrl, W. H. Dip-Coated Silver-Doped $V_2O_5$ Xerogels as Host Materials for Lithium Intercalation. *Solid State Ionics* **1997**, *100*, 247−258.
(31) Giorgetti, M.; Berrettoni, M.; Smyrl, W. H. Doped $V_2O_5$-Based Cathode Materials: Where Does the Doping Metal Go? An X-ray Absorption Spectroscopy Study. *Chem. Mater.* **2007**, *19*, 5991−6000.
(32) Yi, R.; Zai, J.; Dai, F.; Gordin, M. L.; Wang, D. Improved Rate Capability of Si−C Composite Anodes by Boron Doping for Lithium-Ion Batteries. *Electrochem. Commun.* **2013**, *36*, 29−32.
(33) Lin, Q.; Xu, Y.; Fu, E.; Baber, S.; Bao, Z.; Yu, L.; Deng, S.; Kundu, J.; Hollingsworth, J.; Bauer, E.; McCleskey, T. M.; Burrell, A. K.; Jia, Q.; Luo, H. Polymer-Assisted Chemical Solution Approach to $YVO_4$:Eu Nanoparticle Networks. *J. Mater. Chem.* **2012**, *22*, 5835−5839.
(34) Fei, L.; Lin, Q.; Yuan, B.; Chen, G.; Xie, P.; Li, Y.; Xu, Y.; Deng, S.; Smirnov, S.; Luo, H. Reduced Graphene Oxide Wrapped FeS Nanocomposite for Lithium-Ion Battery Anode with Improved Performance. *ACS Appl. Mater. Interfaces* **2013**, *5*, 5330−5335.
(35) Ko, Y. N.; Chan Kang, Y.; Park, S. B. A New Strategy for Synthesizing Yolk-Shell $V_2O_5$ Powders with Low Melting Temperature For High Performance Li-Ion Batteries. *Nanoscale* **2013**, *5*, 8899−8903.
(36) Wang, Y.; Zhang, H. J.; Lim, W. X.; Lin, J. Y.; Wong, C. C. Designed Strategy to Fabricate a Patterned $V_2O_5$ Nanobelt Array as a Superior Electrode for Li-Ion Batteries. *J. Mater. Chem.* **2011**, *21*, 2362−2368.